RSC Advances

PAPER

View Article Online
View Journal | View Issue

Cite this: *RSC Adv.*, 2025, **15**, 29528

Synergistic effects of hydroxylation and structural defects in hexagonal boron nitride for dye removal from wastewater

Abdullah-Al Noman,[a] Kishan Nandi Shoudho,[a] Zayed Bin Zakir Shawon,[b] Mohammad Khurshed Alam,[c] Shoeb Ahmed[a] and Iftheker Ahmed Khan *[a]

Hexagonal boron nitride (h-BN) was structurally modified using a simple and efficient chemical weathering method and assessed for its ability to remove anionic Congo Red (CR) and cationic Neutral Red (NR) dyes from wastewater. Batch sorption experiments explored variables including solution pH (2–12), modified h-BN dosage (0.25–1.0 g L^{-1}), contact time (10–420 min), and dye concentration (10–500 mg L^{-1}). Detailed characterization revealed the integration of hydroxyl groups, distinctive rough and cracked surfaces, increased interlayer spacing and crystal size, monodispersed stable solution, and enhanced solubility of modified h-BN. Optimal dye removal occurred at 0.5 g per L dosage, with CR achieving 99.23 ± 0.06% efficiency at pH 2 (60–90 min) and NR 85.77 ± 1.51% at pH 11 (90–120 min) in deionized water. Electrostatic interactions between the modified h-BN and dye molecules drove pH-dependent adsorption, following a pseudo-second-order kinetics model, indicative of chemisorption. Langmuir isotherms confirmed monolayer adsorption on homogeneous surfaces. For similar parameters, in a mixed dye system (*i.e.*, CR : NR = 1 : 1), the removal efficiency favored at pH = 2 over pH = 11 (*i.e.*, 80.54 ± 1.16% over 60.83 ± 5.18%)—was less than mono-dye systems—which indicates that more CR dye could be removed with the exact adsorbent dosage. A limited study was performed with clarifier inlet textile wastewater, which showed a decrease in removal efficiency compared to deionized conditions. A steady decrease in removal efficiency was observed while performing adsorption–desorption cycles. The results demonstrate the potential of modified h-BN as an adsorbent in dye removal from industrial wastewater.

Received 28th May 2025
Accepted 11th August 2025

DOI: 10.1039/d5ra03754a

rsc.li/rsc-advances

1 Introduction

The meteoric expansion of the textile industry has led to increased use of raw materials, including fabrics, dye, and water. Generally, textile wastewater contains cationic and anionic dyes primarily used for dyeing nylon, acrylic, silk, and wool fibers.[1] The dye concentration of textile effluent varies across different types of production units. Even though some high values of dye concentration have been reported in the literature, the usual textile dye concentration of 10–50 mg L^{-1} in the clarifier outlet is considered a standard one.[2,3] Despite the textile sector's significant contribution to the economy of Bangladesh, the sector's reliance on toxic and carcinogenic substances, particularly synthetic dyes, including azo, vat, reactive, and disperse dyes, poses a serious concern for environmental degradation.[4] Without adequate treatment, the textile industry's wastewater is frequently released into the environment, significantly impacting and creating freshwater scarcity. Hence, developing sustainable and efficient water treatment technologies has become necessary. Multiple treatment approaches have been developed globally to manage dye-containing wastewater sustainably. While the primary and secondary treatment stages have been well-established through extensive research, including chemical processes in coagulation–flocculation tanks and biological methods in clarifier tanks, the tertiary or advanced treatment stage remains an active area of research crucial for achieving sustainable management of water pollution.[4] This research focuses on the adsorption process, a component of tertiary treatment, specifically for treating dye-contaminated wastewater due to its economic feasibility, recyclability potential, suitability for large-scale applications, and operational simplicity.[5]

Crystal violet, Basic Blue, Basic Red, Methylene Blue (MB), and Neutral Red (NR) are some examples of cationic dyes that have been extensively employed as model dyes in adsorption research.[6–20] The current study has considered Neutral Red (NR)—a synthetic azo dye with formula $C_{15}H_{17}ClN_4$—commonly

[a]*Department of Chemical Engineering, Bangladesh University of Engineering and Technology, Dhaka-1000, Bangladesh. E-mail: iftheker@che.buet.ac.bd*
[b]*Department of Mathematics and Natural Sciences, Brac University, Dhaka-1212, Bangladesh*
[c]*Department of Physics, Bangladesh University of Engineering and Technology, Dhaka-1000, Bangladesh*

used in the textile industry for its bright red color and water solubility. It shows pH sensitivity, appearing red in acidic conditions and yellow in neutral to alkaline environments. It undergoes single-stage two electron transfer reduction, and can serve as a corrosion inhibitor for carbon steel in acidic media, increasing effectiveness with concentration.[21,22] Cationic textile dyes contain hydrochloride or zinc chloride complexes and cause various health issues, from skin irritation to potential cancer risks.[5] On the other hand, anionic dyes contain negatively charged molecules and include direct and reactive dyes, such as azoic, anthraquinone, and nitro dyes, all characterized by their water-soluble ionic components.[23] While reactive dyes form covalent bonds with materials like cotton and wool, they pose environmental concerns due to their low fixation rates and tendency to hydrolyze in water.[24] Acid dyes, another anionic dye, are commonly used for silk, wool, and synthetic fibers. Although they dissolve well in water, their organic sulphonic acid composition makes them potentially harmful to human health.[25] Congo Red (CR)—with formula $C_{32}H_{22}N_6Na_2O_6S_2$—consists of two azo chromophores and acidic auxochromes (–SO_3H) attached to benzene structures, has a linear symmetrical structure with a hydrophobic center of two phenyl rings connected *via* di-azo linkage and these phenyl rings are linked to two charged terminal naphthalene moieties that contain sulfonic and amino groups.[25] CR exhibits a red color in the basic medium and a blue color in the acidic medium due to its di-azo structure and is widely utilized in pulp, paper, textiles, cosmetics, pigments, leather, pharmaceuticals, *etc.* Its extensive use significantly contributes to industrial pollution and significant health risks due to its cytotoxic, carcinogenic, and mutagenic properties.[25] In brief, anionic diazo dye, such as CR, and cationic dye, such as NR, are extensively used in the textile industry but are significant pollutants in wastewater due to their synthetic origin, toxicity, environmental persistence, and resistance to biodegradation. Both dyes are common pollutants in textile effluents and require effective removal methods, often employing advanced materials like nanoparticles and carbon-based adsorbents. The properties of both dyes are listed in Table S1 of SI, and they were chosen for the current study.

In a system where dye acts as an adsorbate, several forces may be present: van der Waals forces (*i.e.*, attraction and repulsion of molecules), electrostatic interactions (*e.g.*, charged molecules), hydrophobic interactions (*e.g.*, presence of nonpolar molecules), hydrogen bonding (*i.e.*, dipole interaction), and π–π interactions (*e.g.*, presence of aromatic rings).[26] These forces are pertinent when removing them using different adsorbents. Several micro-, meso-, and macro-pores exist in an ideal adsorbent. In addition, an abundance of surface functional groups on the adsorbent surface is believed to boost adsorption effectiveness. Under this circumstance, metallic oxide nanoparticles such as TiO_2, SiO_2, MnO_2, ZnO, and Fe_2O_3, metallic nanoparticles like silver (AgNPs), gold (AuNPs), and boron nitride derivatives, as well as carbonaceous nanomaterials including carbon nanotubes, fullerenes, and graphene have been used extensively for the selective removal of dyes, *e.g.*, methyl blue, methyl orange, Congo red, neutral red, methyl green, and rhodamine B from wastewater.[27,28] Moreover, nanocomposites, biochar, activated carbon, and other biomass-derived adsorbents are also reported to be used successfully to remove dyes from wastewater.[27,28]

Boron nitride (BN) based materials, which share similarities with the carbon family, represent a distinct category of nanomaterials such as nanoflowers, nanosheets, nanotubes, and nanoparticles, and are characterized by their exceptional characteristics, making them highly suitable scaffolds for many applications.[26] In particular, hexagonal boron nitride (h-BN)—consists of stacked atomic layers with alternating boron and nitrogen atoms and physically similar to graphite—have recently attracted significant research interest for its remarkable characteristics—such as high specific surface area (*i.e.*, ~2600 $m^2\ g^{-1}$), low density comparable to graphene (*i.e.*, ~2.1 *vs.* ~2.3 g cm^{-3}), thermal stability (*i.e.*, stable in the air up to ~800–900 °C), mechanical strength (*i.e.*, ~100 GPa), conductivity, and resistance to corrosion and oxidation (*i.e.*, insulating and passivation effects)—which makes them particularly suitable for water treatment applications.[26,29,30] The BN nanosheets (BNNS) are mostly few-layer sheets with thicknesses of 1–2 nm or 3–6 layers.[6,17,18,31] Similar to carbon nanotubes, there are BN nanotubes (BNNT) with a tubular nanostructure of h-BN. Besides, literature reported metal-doped, such as Cu and Ag, BN structure, porous BN, BN carbon nitride (BCN), and BN nanocomposites with different polymers. Specifically, BN materials have demonstrated potential for the removal of contaminants, *i.e.*, organics, pollutants, antibiotics, and heavy metals from aqueous solution, which was primarily attributed to its structure, *i.e.*, bulk π–π bond, coexisting Lewis acidic and basic sites, and pertinent functionalization, *i.e.*, numerous structural defects and addition of functional groups.[26,32–35] BN structures, especially h-BN, have been intensively investigated across multiple fields, including the water–energy–food–environment–health nexus for membrane water filtration, solar cells, batteries, carbon capture, hydrogels, epoxy cement, ceramic oxides, and catalysis.[36–39]

In addition, BN's adaptable nature allows for modifications, further enhancing its potential applications.[29,30] High-quality dispersions are stable and consist mainly of single-layer or few-layer h-BN sheets with large lateral dimensions. This typically requires exfoliating the sheets from bulk h-BN crystals, as the layers naturally stick together due to strong van der Waals forces. The exfoliation and dispersion of h-BN can be achieved through multiple complementary approaches: direct (single/multiple) solvent interactions *via* IPA, ethylene glycol, ethanol/water, *etc.*, covalent surface modifications such as oxidation of B sites, acidic/basic media treatments, stabilization by surfactants or polymers, *e.g.*, poly(vinyl alcohol) and pluronic acid, biomolecule-assisted processes, ionic intercalation, and thermal expansion methods.[30] When using acids and bases, strong protic acids or Lewis bases interact with acidic B sites to protonate and exfoliate the sheets. Additional acids have been utilized as intercalating agents, which may be classified into acids or salts with few exceptions. Intercalating agents play a role in breaking up the h-BN layers by allowing interlaminar expansion and facilitating the process of exfoliation. Ions intercalate between adjacent h-BN sheets and disturb the

interactions between the layers. NaOH solution, NaOH/KOH, and NaOH/LiCl have been used as intercalating agents to exfoliate BN nanoparticles. However, these works were limited to only functionalization and characterization without any application specifically in dye removal processes.[40,41] The current study has considered using NaOH as an intercalating agent to exfoliate pristine h-BN. A summary of earlier works on h-BN dispersions directly by acids, bases, intercalating agents, solvents, and covalent functionalization, and relevant experimental exfoliation and dispersion protocols, including dispersion concentration and stability, are shown in Tables S2–S4 of SI.

It has been established that h-BN can effectively capture cationic and anionic pollutants and remove specifically charged contaminants through functionalization, thereby offering a promising advancement in wastewater treatment methods.[42] For example, the functionalization of h-BN showed an improved ability to adsorb Rhodamine B dye from aqueous solutions.[18,43] Furthermore, BN nanocomposites or BN doped with another metal particle have demonstrated enhanced adsorption capacity and removal of metal ions, such as arsenic and fluoride, from aqueous solutions.[44] While the initial findings are promising, there is a significant knowledge gap in understanding these processes comprehensively. Extensive research is essential to understand the mechanisms and assess their viability for industrial-scale implementation.

h-BN, BNNS, BNNT, BCN, porous BN, BN fiber, h-BN whisker, and metal-BN have been used as adsorbents to remove anionic dyes (*e.g.*, Sunset Yellow FCF, Methyl Orange, and Congo Red) and cationic dyes (Rhodamine B, Methylene Blue, Neutral Red, Indigo Blue, Malachite Green, and Methyl Green) from wastewater.[6–20,31] A wide range of adsorbent dosages, *i.e.*, 20 to 2000 mg L^{-1}, of these BN structures was tested for different adsorption experiments considering the initial dye concentration of 5–300 mg L^{-1} to determine the maximum adsorption capacity of these BN derivates for the removal of dyes and other materials, *e.g.*, heavy metals, and antibiotics. In all cases, there was a strong correlation of solution pH, which dictates the surface charge of BN structures in aqueous solution with types of dyes, *i.e.*, anionic or cationic.[6–20,31]

To understand the adsorption mechanism, the kinetic data were analyzed using different models, such as pseudo-first-order, pseudo-second-order, and intraparticle diffusion models.[45] The pseudo-first-order model is usually applicable only during the initial stages of the adsorption process.[46] However, the pseudo-second-order model effectively characterizes the adsorbate–adsorbent system interactions across the complete contact duration and enables a direct calculation of the initial adsorption rate and the adsorption capacity without identifying any unknown factors.[46,47] A linear relationship between Q_t and $t^{1/2}$ indicates that intraparticle diffusion is the rate-controlling mechanism of the adsorption process thereby, the intraparticle diffusion model describes the time-dependent intraparticle diffusion of adsorbate species, *e.g.*, molecules, ions, and particles, within the adsorbent matrix.[48] Conversely, the presence of multi-linear segments in the plot suggests that the adsorption process is governed by multiple sequential stages, impacting the adsorption process.

Langmuir, Freundlich, and Sips isotherms were reported in the literature to decipher monolayer and/or multilayer adsorption with homogeneous and/or heterogeneous surfaces.[49] The Langmuir and Freundlich isotherm models are based on the assumption of monolayer and multilayer adsorption occurring on homogeneous and heterogeneous adsorbent surfaces, respectively.[50,51] The enthalpy of adsorption is either independent or decreases logarithmically as the fraction of occupied sites on the adsorbent increases in the case of the Langmuir or the Freundlich isotherm models, respectively.[50,51] However, the Sips isotherm combines elements of both the Langmuir and Freundlich isotherms: at low equilibrium adsorbate concentrations, it approaches the Freundlich isotherm, and at high equilibrium adsorbate concentrations, it predicts the monolayer adsorption behavior characteristic of the Langmuir mode.[52,53] For example, cationic Rhodamine B (RhB) and Methylene Blue (MB) dyes were removed by BNNS at pH 8 since the surface charge of BNNS was found to be −25 mV. The adsorption mechanism was Langmuir (*i.e.*, monolayer with homogeneous surface), and the maximum adsorption capacity from the isotherm study was reported to be 313 and 333 mg g^{-1} for RhB and MB dyes, respectively. Furthermore, the reaction mechanism was attributed to chemisorption resulting from pseudo-2nd-order reaction kinetics.

Table 1 summarizes cationic and anionic dye removal using BN and its derivatives under different adsorption process parameters. The pristine (or bulk) BN materials were proven less stable in an aqueous medium and less effective in dye removal from contaminated water, necessitating dispersion and exfoliation of BN, *i.e.*, h-BN for the current study, *via* different processes such as using solvents, acids/bases, intercalating agents, polymers, *etc.* A range of functional groups, specifically acyl (–COR), alkyl (–R), hydroxyl (–OH), amino ($–NH_2$), amine (–NHR), ether (–OR), and halogen (–X) groups, along with heteroatoms have been incorporated in the BN framework *via* chemical functionalization to improve the surface reactivity.[29]

This work evaluated the adsorption performance of structurally modified hexagonal boron nitride (M-hBN) through liquid phase exfoliation using NaOH for selective removal of dyes, *i.e.*, single dye system of either anionic dye (*i.e.*, Congo Red) or cationic dye (*i.e.*, Neutral Red) and mixed dye system (*i.e.*, Congo Red and Neutral Red) from aqueous solutions. Comprehensive material characterizations were conducted to verify the efficacy of the synthesis process. The h-BN after modification, *i.e.*, M-hBN was used for further experiments, starting with finding the solution pH where dye removal efficiency was maximum. Subsequent experiments were conducted to optimize the M-hBN amount, batch adsorption experiment duration, and initial dye concentration. These adsorption process parameter optimization experiments were further utilized to develop kinetic models and isotherm studies. The effectiveness of the M-hBN was assessed through a comparative analysis of dye removal efficiency in both deionized (DI) water and textile wastewater, considering single and mixed dye conditions. In addition, the study evaluated the reusability

Table 1 Dye-contaminated wastewater treatment by BN and its derivatives[a]

S/N	BN structure	Dye	Dye type	Adsorbent dosage (mg L^{-1})	pH	Dye conc. (mg L^{-1})	Max. adsorption capacity (mg g^{-1})	Isotherm model	Kinetics	Ref.
1	h-BN	SF	A	400	—	75	~58 to ~105	Langmuir	PSO	14
2	h-BN	CR	A	500	2	100	620.58 ± 32.07	Langmuir	PSO	This work
3	h-BN	RhB	C	400	—	100	~140 to 208	Langmuir	PSO	14
4	h-BN	MB	C	400	—	50–200	~230	—	—	15
5	h-BN	NR	C	500	11	100	559.38 ± 25.78	Langmuir	PSO	This work
6	BNNS	MO	A	400		110	~575	Freundlich	PSO	31
7	BNNS	RhB	C	250	6.6	5–80	~76	Langmuir	—	18
8	BNNS	RhB	C	400	8	108	~313	Langmuir	PSO	6
9	BNNS	MB	C	400	8	108	~333	Langmuir	PSO	6
10	BNNS	MB	C	1000	—	5–30	~18	Langmuir	PSO	17
11	BNNS	IB	C	1000	—	5–30	~18	Langmuir	PSO	17
12	BCN	NR	C	~90	—	220	~1350	Langmuir	PSO	7
13	BCN	MaG	C	~90	—	120	~1041	Langmuir	PSO	7
14	BCN	MB	C	—	—	136.4	~1220	Langmuir	—	20
15	BCN	BY	C	—	—	101.4	~560	Langmuir	—	20
16	Porous boron carbide	MB	C	2000	—	10 to 50	~189	Langmuir	PSO	16
17	Ag-BN	RhB	C	200	—	100–300	~880	Langmuir	PSO	13
18	Cu-BN	RhB	C	200	—	—	~743	Langmuir	PSO	11
19	Porous BN	CR	A	400	—	150	~1096 (theo.)	Langmuir	PSO	19
20	Porous BN	MG	C	400	—	170	~1203	Langmuir	PSO	19
21	BN fiber	MB	C	240	8	25	~392	Langmuir	—	8
22	h-BN whisker	RhB	C	30	—	3	~210	Langmuir	—	9
23	h-BN whisker	MB	C	20	—	60	~13 973	Langmuir	—	9
24	3D C-BN	CR	A	500	6	50	~307	Langmuir	—	12
25	3D C-BN	MB	C	500	6	50	~408	Langmuir	—	12
26	3D BN architecture	BY	C	400	—	90	~424	Langmuir	—	10
27	3D BN architecture	CR	A	400	—	110	~717	Langmuir	—	10

[a] BN Structure: h-BN = hexagonal Boron Nitride, BNNS = BN Nanosheet, BCN = BN Carbon Nitride; Dye: SY = Sunset Yellow FCF, CR = Congo Red, RhB = Rhodamine B, MB = Methylene Blue, NR = Neutral Red, MO = Methyl Orange, IB = Indigo Blue, MaG = Malachite Green, BY = Basic Yellow-1, MG = Methyl Green; Dye Type: A = Anionic, C = Cationic; Kinetics: PSO = Pesudo-2nd-Order.

potential of the M-hBN to determine its regeneration capacity under DI water conditions. The specific objectives of the current study were to (a) synthesize structurally modified and exfoliated h-BN from pristine h-BN using caustic soda (NaOH), and (b) determine the removal efficiency of cationic and anionic dyes using modified h-BN (*i.e.*, M-hBN) at optimized process parameters' conditions. The research findings are expected to offer input data for a pilot plant study (*i.e.*, scalable industrial processes) on effective dye removal from textile wastewater, offering a practical solution to this growing environmental challenge.

2 Materials and methods

2.1 Materials

All chemicals utilized in this study were of analytical reagent grade. Hexagonal boron nitride (h-BN), ethanol (C_2H_5OH, ≥99.5%, MW: 46.07 g mol^{-1}), and hydrochloric acid (HCl) were procured from Sigma-Aldrich, USA. Congo red ($C_{32}H_{22}N_6Na_2O_6S_2$, MW: 696.665 g mol^{-1}, λ_{max}: 497 nm) and neutral red ($C_{15}H_{17}ClN_4$, MW: 288.78 g mol^{-1}, λ_{max}: 276 nm), both sourced from Loba Chemie Private Limited, India. Sodium hydroxide (NaOH) was procured from Merck Specialties Private Limited, India. All experimental solutions were prepared using deionized (DI) water.

2.2 Synthesis of structurally modified hexagonal boron nitride

In this research, the structural modification was carried out using the method proposed by Gang Zhao *et al.*[40] In brief, 1.5 g h-BN powder was dispersed in a 0.625 M 400 mL sodium hydroxide solution. This mixture was stirred magnetically at 30 °C for 24-h. The solution was then heated at 80 °C until it completely evaporated, yielding a dry compound. This alkaline treatment and evaporation process was repeated three times to ensure complete modification. After the third cycle, the compound was thoroughly filtered to remove excess sodium hydroxide. The final step involved drying the modified product at 80 °C for 12-h, resulting in the structurally modified boron nitride. A schematic representation of the experimental protocol is shown in Fig. S1 of SI.

2.3 Characterization of h-BN and modified h-BN

The surface functional groups of the synthesized materials were detected with the help of Fourier Transform Infra-Red (FTIR) spectroscopy. FTIR spectroscopy was executed with NICOLET iS5, ThermoScientific. A field emission scanning electron microscope (FESEM) was used to determine the morphology of the materials. In contrast, energy dispersive X-ray spectroscopy (EDX) was used to evaluate the compositional analysis of the

material. FESEM and EDX were taken using EVO 18, ZEISS. X-ray diffraction (XRD) was used to determine the crystalline structure of the nickel ferrite nanoparticle using Rigaku Smartlab XRD with Cu Kβ radiation at wavelength $\lambda = 1.54$ nm, scanning range 10°–80°, scanning speed 10° min^{-1} with 40 kV voltage and 40 mA applied current. The average size of the crystals of synthesized particles was calculated using Scherrer correlation as follows (eqn (1)).

$$D = \frac{k\lambda}{\beta \cos \theta} \quad (1)$$

where D is the average crystal size of the synthesized particles, k is Scherrer constant, β is full width at half maximum (FWHM), and θ stands for Bragg's diffraction angle. Dynamic light scattering (DLS) measurements and zeta potential analysis were performed using a Zetasizer Nano ZS instrument (Malvern Instruments Ltd, UK). The dye concentration in the aqueous solution and solubility of the adsorbent were tested using a UV-vis spectrophotometer (Model: SHIMADZU UV-2600, Japan). The textile wastewater quality parameters, such as pH, dissolved oxygen, total dissolved solids, electrical conductivity, *etc.*, were determined using a multiparameter water quality meter (Model: Hanna HI98194 and SCAN Spectro: lyser V3, Austria).

2.4 Adsorption experiment design

The adsorption efficiency of the dye is dependent on the type and nature of the dye, solution pH, initial dye concentration, and adsorbent dosage.[6] The modified h-BN was used for the CR and NR dye adsorption study. The process was optimized for specific pH, initial dye concentration, adsorption dosage, and duration of dye experiments. Fig. S2 of the SI shows a schematic representation of the experiment design.

2.4.1 Effect of pH. The pH-dependent adsorption behaviors of M-hBN towards Congo Red (CR) and Neutral Red (NR) dyes were evaluated across a pH range of 2–12 (*i.e.*, 2, 4, 6, 8, 10, 11, and 12) at an initial dye concentration of 100 mg L^{-1}, keeping the adsorbent (*i.e.*, M-hBN) dose of 0.5 g L^{-1}. The adsorption process was allowed for a contact time of 480 min to ensure equilibrium. After that, the dye solutions containing the adsorbents were centrifuged for 10 min at 4000 rpm. The supernatant was collected and analyzed for absorbance using a UV-vis spectrophotometer. The dye concentration in the supernatant was determined using a pre-established calibration curve, as presented in Fig. S3 of the SI. The dye removal efficiency, R_e (%), and adsorption capacity, Q_t (mg g^{-1}), for the dye were calculated using eqn (2) and (3), respectively. These equations quantitatively assess the adsorbent's performance in removing dye from the aqueous solution under varying pH conditions.

$$\text{Dye removal efficiency, } R_e(\%) = \frac{(C_o - C_e) \times 100}{C_o} \quad (2)$$

$$\text{Adsorption capacity, } Q_t(\text{mg g}^{-1}) = \frac{(C_o - C_e) \times V}{m} \quad (3)$$

In eqn (2) and (3), C_o and C_e are the initial and equilibrium dye concentrations (mg L^{-1}), respectively; Q_t is the adsorption capacity (mg g^{-1}), V is the solution volume (L), and m is the mass (g) of adsorbents.

2.4.2 Effect of adsorbent dosage. Based on the literature review, three different adsorbent dosages, *i.e.*, 0.25, 0.50, and 1.00 g L^{-1}, were chosen to study the effect of adsorbent dosage on the uptake of dyes.[6,26,54] The adsorption studies for CR and NR were conducted at an optimum pH value of 2 and 11, keeping an initial dye concentration of 100 mg L^{-1}. The adsorption process proceeded until equilibrium was achieved, which was reported to be 480 min for both dyes. After that, the solution containing the adsorbent and dye was centrifuged at 4000 rpm for 10 min. The supernatant was carefully collected, and its absorbance was measured to determine the extent of dye removal. This approach allows for a comprehensive analysis of the effect of adsorbent dosage on the adsorption efficiency of dye.

2.4.3 Kinetics analysis. The kinetic study of dye adsorption onto M-hBN was conducted over a time range of 0–480 min, with measurements taken at specific intervals: 10, 15, 30, 60, 90, 120, 240, and 480 min. The adsorption studies for CR and NR dyes were conducted at an optimum pH value of 2 and 11, with an initial dye concentration of 100 mg L^{-1} and an adsorbent dose of 0.5 g L^{-1}. After completion of each time interval, the solution containing the adsorbent and dye was centrifuged at 4000 rpm for 10 min. The supernatant was carefully collected, and its absorbance was measured to determine the extent of dye removal. Linear forms of pseudo-1st order, pseudo-2nd order, and intraparticle diffusion models are presented in eqn (4)–(6):

$$\log(Q_e - Q_t) = \log Q_e - \frac{k_1 t}{2.303} \quad (4)$$

$$\frac{t}{Q_t} = \frac{1}{k_2 Q_e^2} + \frac{t}{Q_e} \quad (5)$$

$$Q_t = k_{id} t^{0.5} + C \quad (6)$$

where Q_e (mg g^{-1}) is the amount of dye adsorbed at equilibrium, Q_t (mg g^{-1}) is the amount of dye adsorbed over time t (mins), k_1 is the equilibrium rate constant for the pseudo-1st-order process (1/min), k_2 is the equilibrium rate constant for the pseudo-2nd-order process (g mg^{-1} min^{-1}), k_{id} is the intra-particle diffusion rate constant (mg (g^{-1} $min^{-1/2}$)), and C (mg g^{-1}) is a constant related to the thickness of the boundary layer.

2.4.4 Isotherm analysis. The isotherm study of each dye was conducted over an initial dye concentration range of 10–500 mg L^{-1}, with measurements taken at specific concentrations: 10, 20, 30, 50, 75, 100, 150, 250, 400, and 500 mg L^{-1}. The adsorption studies for CR and NR dyes were conducted for 480 min at an optimum pH value of 2 and 11, keeping an adsorbent dose of 0.5 g L^{-1}. After attaining equilibrium for each case, the solution containing the adsorbent and dye was centrifuged at 4000 rpm for 10 min. The supernatant was carefully collected, and its absorbance was measured to determine the extent of dye removal. The adsorption equilibrium data were analyzed by Langmuir, Freundlich, and Sips isotherm models to elucidate the adsorption mechanism.[49] The

maximum theoretical dye adsorption capacity can be determined using eqn (7)–(9) for Langmuir, Freundlich, and Sips isotherm models.

$$\text{Langmuir Isotherm Model}: \ Q_e = \frac{Q_m k_L C_e}{1 + k_L C_e} \quad (7)$$

$$\text{Freundlich Isotherm Model}: Q_e = K_F C_e^{1/n} \quad (8)$$

$$\text{Sips Isotherm Model}: \ Q_e = \frac{Q_m k_S C_e^{\left(\frac{1}{N}\right)}}{1 + k_S C_e^{\left(\frac{1}{N}\right)}} \quad (9)$$

In these models, K_L (L mg^{-1}) is the Langmuir constant, representing the ratio of adsorption to desorption rates K_F (mg g^{-1}). (L mg^{-1})$^{1/n}$ is the Freundlich constant, where n is a dimensionless factor indicating adsorption favorability (when $n > 1$, suggests favorable adsorption), K_S (1/mg) is the Sips equilibrium constant, N is dimensionless heterogeneity factor (which is between 0 and 1; when $N = 1$, the Sips equation simplifies to the Langmuir isotherm), C_e (mg L^{-1}) is the equilibrium adsorbate concentration (in our case, equilibrium dye concentration for CR and NR), Q_m (mg g^{-1}) is the maximum adsorption capacity derived from the model, and Q_e (mg g^{-1}) is the equilibrium adsorption capacity of the adsorbent.

From the Langmuir model, the separation factor, RL, can be calculated using eqn (10),

$$R_L = \frac{1}{1 + K_L C_o} \quad (10)$$

where, C_o (mg L^{-1}) is the initial dye concentration, and K_L (L mg^{-1}) is the Langmuir constant. The dimensionless parameter R_L determines the shape of the isotherm. ($R_L > 1$), indicates unfavorable adsorption, ($R_L = 1$) signifies linear adsorption, ($0 < R_L$) reflects favorable adsorption.[55]

2.4.5 Reusability. Reusability studies were performed to evaluate the regeneration of M-hBN. After the first cycle of the adsorption study (*i.e.*, after 480 min), the collected M-hBN was regenerated using ethanol as the desorbing agent. For the regeneration process, the used M-hBN was stirred in 60 mL of ethanol at 150 rpm for 4 hours. After regeneration, the M-hBN was recovered through centrifugation and reused for the next adsorption cycle. The effectiveness of this regeneration process was determined by comparing the removal efficiency of each subsequent cycle with that of the first cycle.[56]

2.4.6 Mixed dye system. The adsorption efficiency of M-hBN in mixed dye (*i.e.*, CR + NR) systems was performed in two different mediums, *i.e.*, DI water and Textile wastewater collected from the clarifier inlet of a textile ETP. For single-dye systems, solutions of CR and NR were prepared at 100 ppm concentration in both DI water and textile wastewater separately. Additionally, binary dye systems were formulated by combining CR and NR in a 1 : 1 ratio, with each dye maintaining a concentration of 50 ppm in DI water and textile wastewater environments. Preliminary analysis of the collected effluent using a UV-vis spectrophotometer confirmed the absence of both CR and NR dyes, verifying that these were not employed in the facility's manufacturing processes. In summary, the experimental protocol maintained consistent conditions across all sample matrices, employing an M-hBN dosage of 0.5 g L^{-1} for 480 min under both acidic (pH 2.0) and basic (pH 11.0) conditions. This experimental design was uniformly applied across all prepared systems, encompassing single-dye and binary-dye configurations in deionized water and textile wastewater matrices. Following the designated contact period, the supernatant was carefully separated and subjected to UV-vis spectrophotometric analysis to quantify the residual dye concentration, enabling the assessment of adsorption efficiency under various experimental conditions.

3 Results and discussions

3.1 Characterization of synthesized materials

3.1.1 SEM and EDX analysis. Fig. 1 shows the SEM images of pristine h-BN at different magnifications. The low magnification image at 1-μm scale (Fig. 1(a)) provides an overview of the

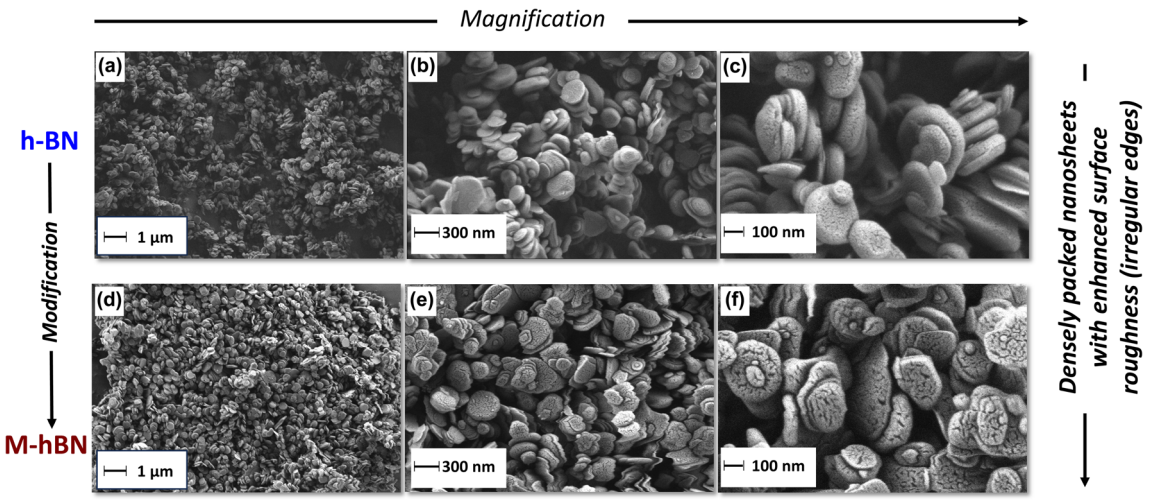

Fig. 1 SEM images of h-BN (a–c) and M-hBN (d–f) at different magnifications.

layered, sheet-like morphology of the bulk h-BN particles, consistent with the observations by Zhang *et al.*[57] and Wang *et al.*[58] At higher magnifications of 300 and 100 nm scale (Fig. 1(b and c)), the bulk h-BN exhibits an opaque, thick-layered structure with relatively smooth surfaces and further reveals the bulk nature and absence of thin, transparent sheets, as reported by Zhi *et al.*[59] for pristine h-BN. In contrast, Fig. 1(d–f) presents the SEM images of M-hBN, showing distinct morphological differences compared to the pristine h-BN. The low magnification image at 1-μm scale (Fig. 1(d)) reveals a more open, porous structure with increased surface roughness, indicating successful modification of the h-BN surface, similar to the findings of Wang *et al.*[58] The sheet-like morphology becomes more apparent at the intermediate magnification of 300 nm (Fig. 1(e)), where the surfaces display unique patterns and textures attributed to the modification process. It highlights the irregular, jagged edges of the modified nanosheets, differing from the smooth edges of pristine h-BN. The high-resolution image (Fig. 1(f)) at 100 nm scale clearly shows the presence of surface defects and irregularities induced by the modification, which is significantly different from the smooth surfaces of pristine h-BN, as reported in the reference papers.[40,59] In summary, the SEM analysis supported by the observations confirms the bulk, layered structure of pristine h-BN and the successful modification of h-BN, which results in thinner nanosheets with increased surface roughness, distinctive surface patterns, and structural defects. The M-hBN exhibits a significantly altered surface morphology compared to the pristine h-BN, indicating effective surface functionalization of the h-BN nanosheets.

The EDX analysis shows that pristine h-BN contains 42.54 and 57.46 wt% boron and nitrogen, respectively, which is close to the theoretical B/N ratio of 1 : 1 in h-BN. However, the M-hBN sample exhibits notable changes with reduced B (41.21 wt%) and N (52.74 wt%) content, alongside the introduction of oxygen (O) (6.04 wt%), which suggests successful surface modification or functionalization of the h-BN structure, possibly through chemical treatment or surface oxidation processes. The slight deviation from the original B/N ratio and the incorporation of the 'O' group could indicate potential changes in the material's surface properties. The corresponding elemental mapping is shown in Fig. S4 of the SI.

3.1.2 FTIR analysis. FTIR spectroscopy analyzed the structural difference between pristine and modified h-BN, and the spectra are shown in Fig. 2(a).[60] The pristine sample shows characteristic peaks at ~1335 cm^{-1} and ~758 cm^{-1} wavelength, representing in-plane B–N stretching and out-of-plane B–N bending vibrations, respectively. However, these peaks are shifted to ~1370 cm^{-1} and ~768 cm^{-1} for structurally modified h-BN. The enhanced B–N stretching and bending indicate the thinning of h-BN after exfoliation. FTIR spectra for structurally modified nanomaterials (*i.e.*, M-hBN) exhibit a characteristic peak at ~3464 cm^{-1}, which is similar to the literature-reported (*i.e.*, ~3400–3500 cm^{-1}) stretching vibration of hydroxyl (–OH) groups.[61] This also corroborates the theoretical study on band gap engineering of functionalization of h-BN sheets with hydroxyl groups Bhattacharya *et al.*[61] In addition, the intensity

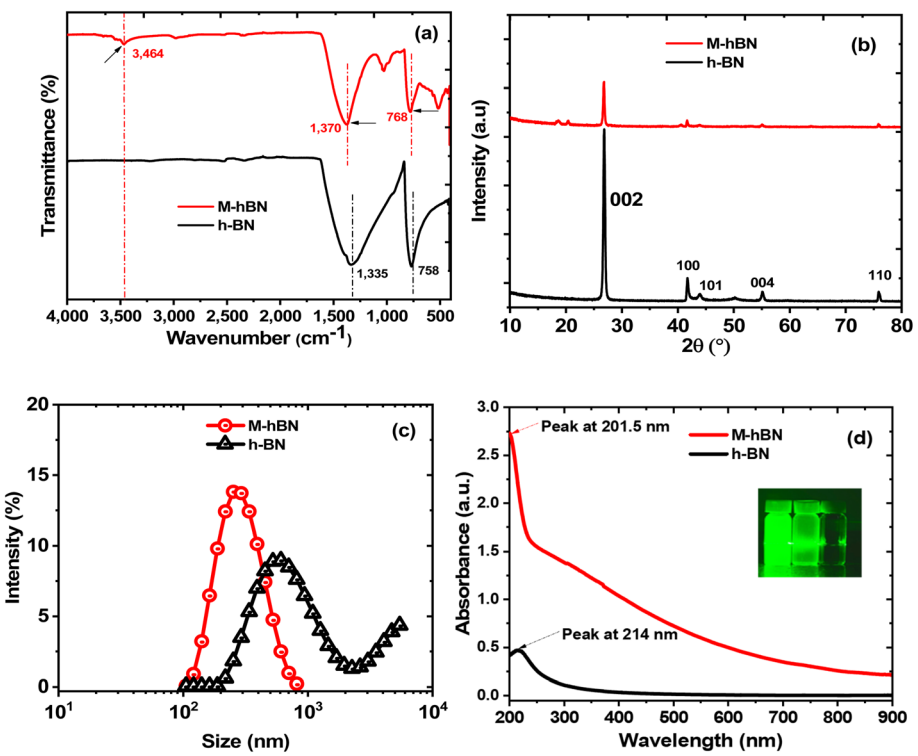

Fig. 2 (a) FTIR spectra, (b) XRD patterns, (c) hydrodynamic size, and (d) UV-vis absorption spectra (inset photograph demonstrating the Tyndall effect) of h-BN and M-hBN.

ratio of the peaks at ~3464 cm^{-1} and 1370 cm^{-1} in M-hBN is much larger than that in h-BN, indicating that h-BN was successfully functionalized with hydroxyl groups.[57] In brief, FTIR spectroscopic investigation corroborates the successful surface functionalization of hexagonal boron nitride, as evidenced by introducing a hydroxyl group while maintaining the fundamental B–N bonding structure.

3.1.3 XRD analysis. The XRD patterns reveal significant structural characteristics of pristine h-BN and M-hBN samples, shown in Fig. 2(b). Both materials exhibit the characteristic hexagonal phase at (002) crystallographic plane. The peak position remains unchanged in both materials in terms of a diffraction angle (*i.e.*, $2\theta = 26.8°$) and shape (*i.e.*, visual observation), suggesting that the exfoliation process did not damage the crystalline structure of the pristine material. Thereby, M-hBN retained the high crystalline structure of the h-BN.[62,63] However, the interlayer spacing of M-hBN expanded compared with h-BN (*i.e.*, 0.242 nm *vs.* 0.210 nm at d002), which indicates successful intercalation while maintaining the fundamental hexagonal structure. The crystallite size—measured using the Scherrer equation—increased from 15.56 nm to 46.60 nm for h-BN and M-hBN samples, supported by previous works.[58,63] Furthermore, the reduced intensity and sharpness of diffraction peaks at higher angles assigned to the (100), (101), and (004) planes indicate long-range crystalline order and weakened *c*-direction stacking (perpendicular to the BN layers).[58,62] In brief, XRD analysis suggests that the modification process effectively expands the crystallite size and interlayer spacing of M-hBN while preserving the essential crystalline characteristics of h-BN.

3.1.4 DLS analysis. The hydrodynamic size of h-BN and M-hBN at aqueous conditions (*i.e.*, DI water) is found to be 765 nm and 266 nm with polydispersity indices (PDI) of 0.404 and 0.07, respectively, *via* DLS analysis; shown in Fig. 2(c). These results indicate successful exfoliation and uniform dispersion of M-hBN. The size distribution of M-hBN shows a predominant single peak, suggesting the presence of well-dispersed nanosheets. This result is comparable to previous studies where functionalized BN nanosheets showed effective hydrodynamic diameters around 334 nm and a low polydispersity value of 0.051.[63] The narrow size distribution and low PDI value confirm that the surface modification effectively prevents significant aggregation in the aqueous medium, consistent with the enhanced colloidal stability reported for functionalized h-BN systems.

3.1.5 UV-visible absorption spectra and Tyndall effect. The solubility and dispersion stability of pristine and hydroxylated h-BN, *i.e.*, h-BN and M-hBN, were investigated using optical absorption spectroscopy, a suitable approach given the inherent superhydrophobicity and poor aqueous solubility of h-BN. Both materials exhibit a strong absorption peak in the deep ultraviolet (UV) region (~200–220 nm), corresponding to their intrinsic bandgap and originating from interband transitions between the valence and conduction bands. As shown in Fig. 2(d), the absorption peaks are distinctly observed at 214 nm for h-BN and 201.5 nm for M-hBN, respectively. The blue shift (214 nm → 201.5 nm) and the corresponding increase in bandgap (5.79 eV → 6.15 eV) are attributed to structural and electronic modifications induced by hydroxylation and exfoliation, as confirmed by FTIR spectroscopy.[40,60,63,64] These changes contribute to the enhanced dispersion stability of M-hBN in aqueous media. This trend is consistent with previous reports on hydroxylated h-BN, where similar blue shifts were observed—*e.g.*, Ren *et al.* (2021) at 200–202 nm, Wang *et al.* (2018) at 204.8 nm, and Nazarov *et al.* (2012) at 196–206 nm.[18,63,65] Further evidence of improved dispersibility was provided by the Tyndall effect observed in M-hBN dispersions, where laser light scattering confirmed the formation of a stable colloidal suspension—a behavior also reported in other functionalized h-BN.[66] This enhanced stability is particularly advantageous for practical applications requiring uniform aqueous dispersions, such as polymer nanocomposites and optical limiting.[40,63]

3.2 Optimization of process parameters

3.2.1 Effect of variation of pH. Fig. 3 represents the pH-dependent removal efficiency and adsorption capacity of CR and NR dyes using M-hBN. For CR dye, the removal efficiency exhibits maximum performance at acidic pH 2 (99.23 ± 0.06%), followed by a sharp decline to 69.73 ± 2.00% at pH 4, and further decreases to approximately 23.80 ± 1.85% at pH 12. Conversely, NR removal efficiency demonstrates an opposite trend, increasing from 35.13 ± 0.60% at pH 2 to 85.77 ± 1.51% at pH 11, maintaining high efficiency (85.77 ± 1.51%) at pH 11 and 12. Similarly, the adsorption capacity (Q_e) of CR dye exhibits a significant decreasing trend as pH increases, with maximum adsorption capacity observed at pH 2 (199.12 ± 0.23 mg g^{-1}) and minimum at pH 8 (37.20 ± 3.19 mg g^{-1}). Conversely, NR demonstrates increasing adsorption capacity with increasing

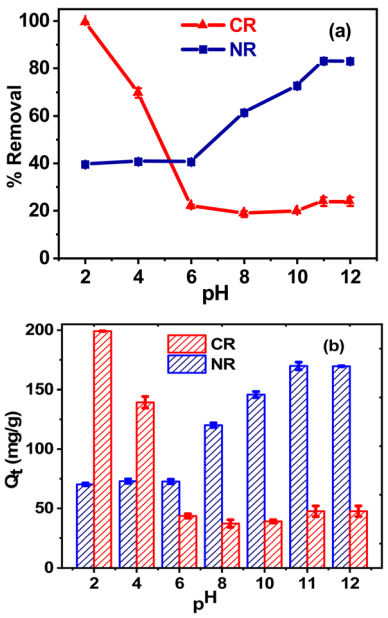

Fig. 3 pH-dependent (a) removal efficiency and (b) adsorption capacity.

pH, reaching optimal performance at pH 11 (169.80 ± 3.15 mg g^{-1}).

The zeta potential of M-hBN is +0.182 mV at pH 2, indicating a slightly positive surface charge that facilitates the adsorption of the negatively charged anionic dye, CR, through electrostatic attraction, resulting in high removal efficiency. As the pH increases to neutral pH, the surface charge becomes negative (zeta potential = −22.5 mV), causing electrostatic repulsion with CR and reducing its removal efficiency.[67] Conversely, at high pH levels (alkaline conditions, *e.g.*, pH = 11), the adsorbent M-hBN surface becomes more negatively charged, evident from the zeta potential value of −42.8 mV. For the current study, this increased surface charge, *i.e.*, from −22.5 to −42.8 mV, enhances the electrostatic attraction of the adsorbent with positively charged cationic dyes, particularly the NR dye.

This may be why the removal efficiency is reduced from (99.23 ± 0.06%), at low pH to 23.80 ± 1.85% at high pH value for CR dye. For NR dye, pH increases from pH 2 to 12, and increasing electrostatic attraction between adsorption sites and NR cations causes an increase in NR removal and adsorption capacity. As the pH decreases, the adsorbent surface becomes increasingly saturated with protons, causing the NR cations to compete with hydrogen ions for adsorption sites, reducing adsorption capacity. This is likely due to the build-up of NR cations at the interface, resulting in a positive charge on the surface that hinders further adsorption of NR cations, thus decreasing the removal efficiency.[68] As reflected in the zeta potential data and corresponding graph, the removal efficiency trends for both dyes confirm that M-hBN's adsorption is governed by electrostatic interactions, making it highly effective for selective dye removal based on pH adjustments.

3.2.2 Effect of variation of adsorbent dosage. The dye adsorption capacity and subsequent dye removal efficiency of M-hBN in the DI water system for both dyes were studied using adsorbent dosages ranging from 0.25 to 1.0 g per L solution, maintaining 100 ppm dye conc. In the case of CR and NR dyes—shown in Fig. 4—it was observed that the adsorption capacity decreased from 325.7 ± 2.79 mg g^{-1} to 99.7 ± 0.03 mg g^{-1} and 261.37 ± 19.15 mg g^{-1} to 89.0 ± 2.36 mg g^{-1}, respectively, as the adsorbent dosage increased from 0.25 to 1.0 g L^{-1}. However, the dye removal efficiency increased from 81.43 ± 0.57% to 99.23 ± 0.06%, and from 65.35 ± 4.78% to 89.0 ± 2.36% for CR and NR dyes, respectively, over the same range of initial adsorbent dosage. At low dosages, say up to 0.5 g L^{-1}, increasing the amount of adsorbent typically offers increased surface area, hydroxyl function groups, active sites, and greater availability of unsaturated adsorption sites available for adsorption, which leads to significant removal efficiency. The removal efficiency doesn't change significantly beyond 0.5 g per L dosage due to a decrease in adsorption capacity at higher dosages. Several factors, such as aggregation/agglomeration of adsorbent particles, overlapping of adsorption sites, increase in diffusion path length, *etc.*, at higher dosages, may contribute to this.[69,70]

The gradual increase of adsorbent increases the total dye removal (*i.e.*, 65.34 to 85.77 to 89.00 mg NR dye per L solution). Still, the incremental increase of this dye removal is not that significant (*i.e.*, 31.27% and 36.20% for 0.5 and 1.0 g L^{-1} compared to 0.25 g per L dosage). This is reflected in the equilibrium adsorption capacity (*i.e.*, as per eqn (3)), which decreases with increased adsorbent dosage for both dyes. For the subsequent experiments, an adsorption dosage of 0.5 g L^{-1} was considered. This study generally reveals an inverse relationship between adsorption capacity (Q_e) and adsorbent dosage, while removal efficiency positively correlates with adsorbent dosage. Similar results have been found for different dyes using similar adsorbents, such as RhB and MB removal using BNNS,[6] MB and MO removal using functionalized graphene oxide sheets,[54] CR removal using Zinc peroxide nanomaterial,[71] and NR removal using halloysite nanotubes from an aqueous solution.[68]

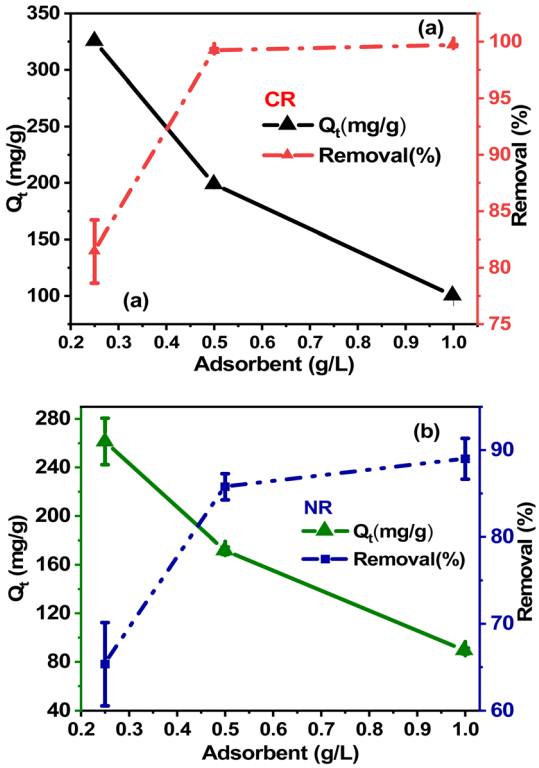

Fig. 4 Effect of adsorbent dosage on dyes' adsorption capacity and removal efficiency: (a) CR and (b) NR dyes.

3.2.3 Effect of variation of contact time. The time-dependent adsorption behavior of dye onto M-hBN was systematically investigated under optimized conditions. Both dyes exhibited characteristic two-phase adsorption kinetics: a rapid initial uptake followed by a gradual approach to equilibrium, shown in Fig. 5. For CR, the adsorption capacity increased dramatically from 0 to 144.91 ± 8.64 mg g^{-1} within the first 10 min, followed by a steady increase to 186.84 ± 2.67 mg g^{-1} at 30 min, ultimately reaching equilibrium at 198.82 ± 0.09 mg g^{-1} after 60–90 min. Similarly, NR demonstrated rapid initial uptake, reaching 135.23 ± 13.28 mg g^{-1} in the first 10 min, followed by a gradual increase to 147.98 ± 9.79 mg g^{-1} at 30 min, achieving equilibrium at 172.57 ± 1.62 mg g^{-1} after 120 min. For 10 to 15 minutes, rapid adsorption occurs due to more active sites, which are easily

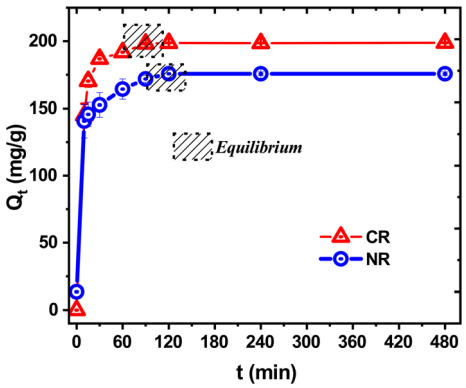

Fig. 5 Effect of contact time on the adsorption capacities (Q_t).

available for the adsorption on the M-hBN. Consequently, M-hBN can easily interact with dyes without hindrance in the initial stage. With an increase in interaction time, adsorption slows down, which implies the utilization of available active sites for adsorption, thereby the active site becomes saturated.[6] When adsorption is controlled by pore diffusion, reaching equilibrium requires significantly more time. Thus, the rapid adsorption of CR and NR suggests that chemical interactions play a key role in the adsorption process.

3.2.4 Effect of initial dye concentration. The equilibrium adsorption capacities (Q_e) of M-hBN increase steadily with lower initial dye concentration ranges (*i.e.*, 10 to 250 mg L^{-1}), as shown in Fig. S5 of SI, which is attributed to the enhanced mass transfer process from the interaction of dye molecules with the adsorbent.[72] At dye concentrations exceeding 250 mg L^{-1}, the ratio of available active sites on the adsorbent surface to the number of CR or NR molecules decreases. This imbalance slows the mass transfer rate, eventually reaching adsorption saturation[73] at a higher concentration range (*i.e.*, 300–500 mg L^{-1}). Therefore, CR showed ~17.7% higher uptake than NR for the same adsorbent, considering the maximum adsorption capacity of CR and NR are 620.59 ± 32.07 mg g^{-1} and 559.39 ± 25.78 mg g^{-1}, respectively. As indicated by standard deviations, the experimental uncertainty remained notably low (<2%) at concentrations below 150 mg L^{-1} for both dyes but increased at higher concentrations, particularly above 400 mg L^{-1}. The distinct optimal pH conditions (CR at pH 2 and NR at pH 11) suggest different binding mechanisms dominated by electrostatic interactions. The superior performance of CR adsorption likely stems from more favorable molecular interactions and better accessibility to binding sites. These findings indicate that the optimal operating range for practical applications lies between 200–300 mg L^{-1}, where capacity utilization and removal efficiency are maximized. At dye concentrations exceeding 250 mg L^{-1}, the ratio of available active sites on the adsorbent surface to the number of CR or NR molecules decreases. This imbalance slows the mass transfer rate, eventually reaching adsorption saturation.[73]

3.3 Comparison of adsorption capacities for different adsorbents

M-hBN demonstrated exceptional adsorption capacities for both NR and CR dyes, surpassing all compared adsorbents. Considering the removal of CR dye, M-hBN adsorbent reaches an (experimental) adsorption capacity of 620.59 ± 32.07 mg g^{-1}, which is 1.8–18 times higher than adsorbents such as porous γ-alumina nanoshells (*i.e.*, 370.4 mg g^{-1}), coal-based mesoporous adsorbents (*i.e.*, 189 mg g^{-1}), and Na-bentonite (*i.e.*, 35.84 mg g^{-1}).[74–76] Similarly, for the removal of NR dye, M-hBN adsorbent achieves (experimental) maximum adsorption capacity of 559.39 ± 25.78 mg g^{-1}, outperforming materials like halloysite nanotubes (*i.e.*, 54.85 mg g^{-1}), Fe_3O_4 hollow nanospheres (*i.e.*, 105 mg g^{-1}), and Mn-impregnated activated carbons (*i.e.*, 217.39–285.71 mg g^{-1}) by 2–10 times.[68,77,78] Details in Table S5 of SI. This remarkable performance is attributed to the structural modifications of h-BN, enhancing its surface area, functional groups, and electrostatic interactions. These findings establish M-hBN as a highly efficient and competitive adsorbent for cationic and anionic dyes, making it a promising candidate for wastewater treatment applications.

3.4 Kinetics study

The kinetic behaviors of dye adsorption were investigated from the data collected to study the effect of contact time on adsorption capacity. Several models outlined in the literature section, such as pseudo-first-order, pseudo-second-order, and intraparticle diffusion models, are fitted and shown in Fig. 6. The corresponding model-fitted data are listed in Table 2. Kinetics modeling parameters for CR and NR dyes. The

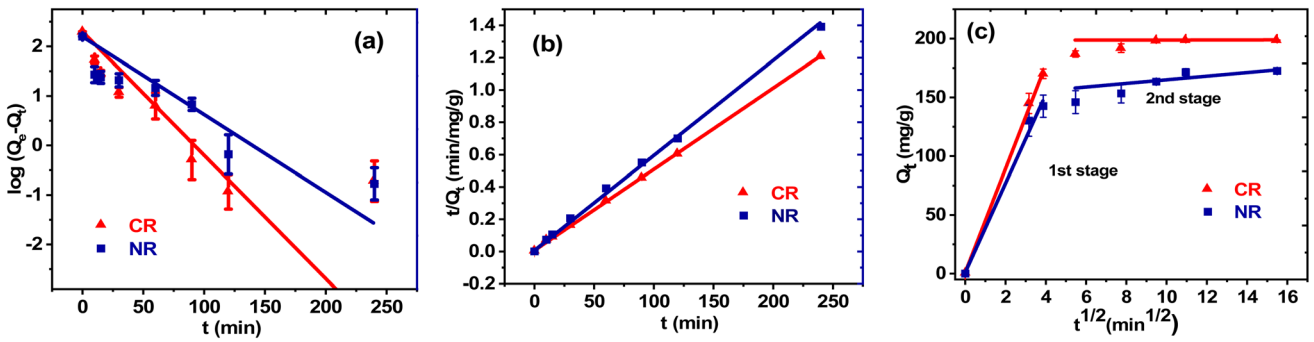

Fig. 6 Investigation of (a) pseudo-first-order kinetic, (b) pseudo-second-order kinetic, and (c) intraparticle diffusion model behavior.

Table 2 Kinetics modeling parameters for CR and NR dyes

Model		CR at pH = 2			NR at pH = 11		
Pseudo-1st-order kinetics		$R^2 = 0.73$	Q_c, calc. = 37.65	$K_1 = 0.029$	$R^2 = 0.89$	Q_c, calc. = 61.74	$K_1 = 0.024$
Pseudo-2nd-order kinetics		$R^2 = 0.99$	Q_c, calc. = 200	$K_2 = 2.45 \times 10^{-3}$	$R^2 = 0.99$	Q_c, calc. = 175.43	$K_2 = 1.44 \times 10^{-3}$
Intraparticle diffusion model	1st stage	$R_1^2 = 0.99$	$C_1 = 2.4 \times 10^{-4}$	$K_{id1} = 44.18$	$R_1^2 = 0.99$	$C_1 = 2.4 \times 10^{-4}$	$K_{id1} = 37.93$
	2nd stage	$R_2^2 = 0.005$	$C_2 = 198.09$	$K_{id2} = 0.02$	$R_2^2 = 0.70$	$C_2 = 149.36$	$K_{id2} = 1.54$

Parameter (Unit): Q_c, calc. (mg g^{-1}); K_1 (1/min); K_2 (g mg^{-1} min^{-1}); C_1 and C_2 (mg g^{-1}); K_{id} (mg g^{-1} min$^{1/2}$)

adsorption studies in consideration do not fit (*i.e.*, $R^2 = 0.73$ and 0.89 for CR and NR dyes) significantly well with the pseudo-first-order model. The intraparticle diffusion analysis revealed a two-stage adsorption process: an initial rapid uptake phase (0–4 min$^{1/2}$) followed by a slower second stage (4–16 min$^{1/2}$). The value of R^2 for the 1st stage of the intraparticle diffusion model equals 0.99, indicating diffusion may be controlled by boundary layer diffusion and surface adsorption. However, the values of R^2 for the 2nd stage of the intraparticle diffusion model equal 0.005 and 0.70 for CR and NR dyes, respectively. This indicates little or no intraparticle diffusion in pores.[79] Thereby, it can be inferred that the adsorption of CR and NR hardly follows the intra-particle diffusion model.[80] Interestingly, the pseudo-second-order model provided the best fit for both dyes (*i.e.*, $R^2 = 0.99$). This indicates chemisorption as the rate-limiting step for the adsorption of dye on the adsorbent, with CR showing a higher rate constant (*i.e.*, $k_2 = 2.45 \times 10^{-3}$ g mg^{-1} min^{-1}) compared to NR (*i.e.*, $k_2 = 1.44 \times 10^{-3}$ g mg^{-1} min^{-1}). The kinetics studies reveal that CR dye demonstrated superior performance with a higher equilibrium capacity (200 mg g^{-1}) than NR dye (175.43 mg g^{-1}), reaching equilibrium more rapidly while considering M-hBN as an adsorbent. The strong alignment of kinetic data with the pseudo-second-order model indicates that the adsorption of CR and NR on M-hBN is best described by this model, which assumes chemisorption as the rate-limiting step throughout the adsorption process.

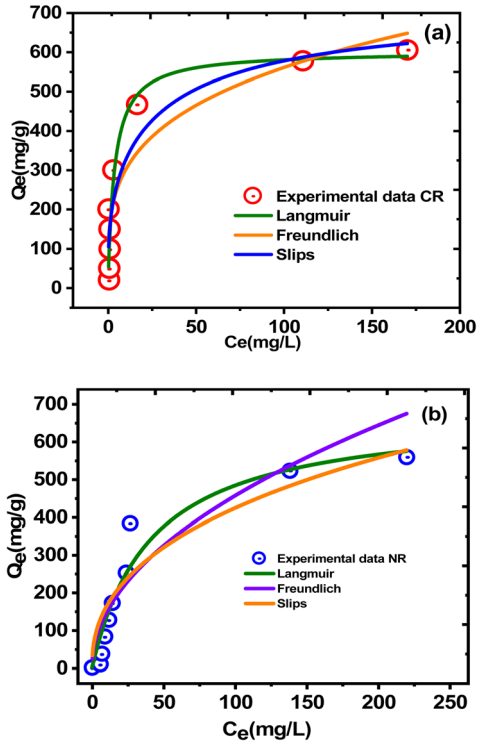

Fig. 7 Isotherm Models for (a) CR and (b) NR dyes.

3.5 Isotherm study

The adsorption behavior of dyes was systematically evaluated using three isotherm models, and the corresponding data are presented in Fig. 7 and Table 3, respectively. The Langmuir isotherm for CR at pH 2 showed a correlation ($R^2 = 0.96$) with a maximum adsorption capacity (Q_{max}) of 602.06 mg g^{-1}, experimentally found 620.59 ± 32.07 mg g^{-1}, and R_L value from 0.0093 to 0.321. In contrast, NR at pH 11 demonstrated strong fitting ($R^2 = 0.97$) with a maximum adsorption capacity Q_{max} of 590.02 mg g^{-1}, experimentally found 559.39 ± 25.78 mg g^{-1}, and R_L value from 0.07662 to 0.8058. For each case, $0 < R_L < 1$ indicates that the adsorption of CR and NR onto M-hBN is favorable.[81]

The Freundlich isotherm parameters for CR at pH 2 ($R^2 = 0.85$) revealed $K_F = 159.31$ and $n = 3.66$. Whereas for NR at pH 11 ($R^2 = 0.83$), $K_F = 46.51$ and $n = 2.408$. For both of dyes, the n values are >1, which indicates that the adsorption of CR and NR is favorable. The Sips isotherm model for CR at pH 2 showed a correlation ($R^2 = 0.88$) with $Q_S = 717.56$ mg g^{-1}, $K_S = 0.029$, and $N = 0.35$. Sips isotherm model for NR at pH 11 exhibited the fit ($R^2 = 0.89$) with $Q_S = 1467.76$ mg g^{-1}, $K_S = 0.0012$, and $N_s = 0.427$. For both cases, Q_s deviated from the experimental value. The isotherm analysis revealed strong alignment with the Langmuir model for both dyes. Congo Red (CR) exhibited a high correlation coefficient ($R^2 = 0.96$) with a theoretical maximum adsorption capacity (Q_{max}) of 602.06 mg g^{-1}, closely matching the experimental value of 620.59 ± 32.07 mg g^{-1}. Similarly, Neutral Red (NR) demonstrated excellent fit ($R^2 = 0.97$) with a theoretical Q_{max} of 590.02 mg g^{-1} corresponding to the experimental value of 559.39 ± 25.78 mg g^{-1}. These results confirm monolayer adsorption on a homogeneous surface for both dyes.

3.6 Reusability

Fig. 8 represents the regeneration study of the adsorbent, demonstrating notably different performance patterns for Congo Red (CR) and Neutral Red (NR) dyes across seven consecutive adsorption–desorption cycles. At pH 2, it exhibited superior initial efficiency (99.23 ± 0.06%) compared to NR at pH 11 (85.77 ± 1.51%), maintaining this advantage throughout all

Table 3 Langmuir, Freundlich and Sips isotherm data for CR and NR

Adsorption isotherms	CR at pH = 2			
Langmuir isotherm	$R^2 = 0.96$	$Q_{max} = 602.06$ mg g^{-1}	$k_L = 0.264$	
Freundlich isotherm	$R^2 = 0.85$	$K_F = 159.31$	$n = 3.66$	
Sips isotherm	$R^2 = 0.88$	$Q_S = 717.56$ mg g^{-1}	$K_S = 0.029$	$N = 0.35$
Adsorption isotherms	NR at pH = 11			
Langmuir isotherm	$R^2 = 0.97$	$Q_{max} = 590.02$ mg g^{-1}	$k_L = 0.0241$	
Freundlich isotherm	$R^2 = 0.83$	$K_F = 46.51$	$n = 2.408$	
Sips isotherm	$R^2 = 0.89$	$Q_S = 1467.7$ mg g^{-1}	$K_S = 0.0012$	$N_s = 0.427$

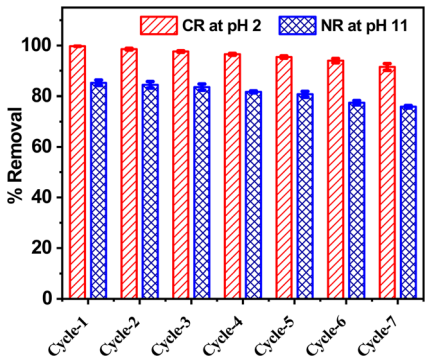

Fig. 8 Reusability efficiency of M-hBN.

cycles. Both dyes showed a gradual efficiency decline, with CR experiencing an 8.20% total decrease (average 1.37% per cycle) to reach 91.49 ± 1.31% by cycle 7. In comparison, NR demonstrated a slightly steeper 9.34% total reduction (average 1.56% per cycle), reaching 75.89 ± 0.50%. The performance gap between CR and NR widened marginally from 14.45% to 15.60% over the seven cycles, with CR maintaining industrially viable removal efficiency above 90% throughout. Statistical analysis revealed minimal standard deviation overlap, confirming significant performance differences between the dyes. Notably, CR exhibited increasing performance variability in later cycles (particularly cycle 7), suggesting potential adsorbent degradation, while NR showed more consistent but larger standard deviations throughout. Despite gradual degradation, the sustained high performance of CR above 90% efficiency across all cycles indicates strong potential for industrial applications. However, replacement after 5–6 cycles may be optimal for NR applications when efficiency drops below 80%. Ethanol washing was applied after each cycle to dissolve the captured species and regenerate the sorption sites. However, complete regeneration may not have been achieved, gradually reducing removal efficiency over successive cycles. Nevertheless, the efficiency retention remained significant even after seven cycles.

3.7 Dye removal efficiency in mixed dye system

The viability of the synthesized functionalized hexagonal boron nitride for removing CR and NR from DI water and textile wastewater, with mixed dye system effects. The textile wastewater and DI water characteristics were measured and tabulated in Table S6 of the SI. In brief, textile wastewater had high TDS, TSS, and COD values compared to DI water. Fig. 9(a) demonstrates varying removal efficiencies of CR under different conditions. In DI water, CR alone showed the highest removal efficiency at 99.23 ± 0.06%, exhibiting remarkable consistency as indicated by the extremely small error bar. When the same concentration of CR was tested in textile wastewater, the removal efficiency slightly decreased to 93.85 ± 3.95%. The larger error bar in this condition suggests more variability in the removal process, possibly due to the complex matrix of textile wastewater interfering with the adsorption mechanism.

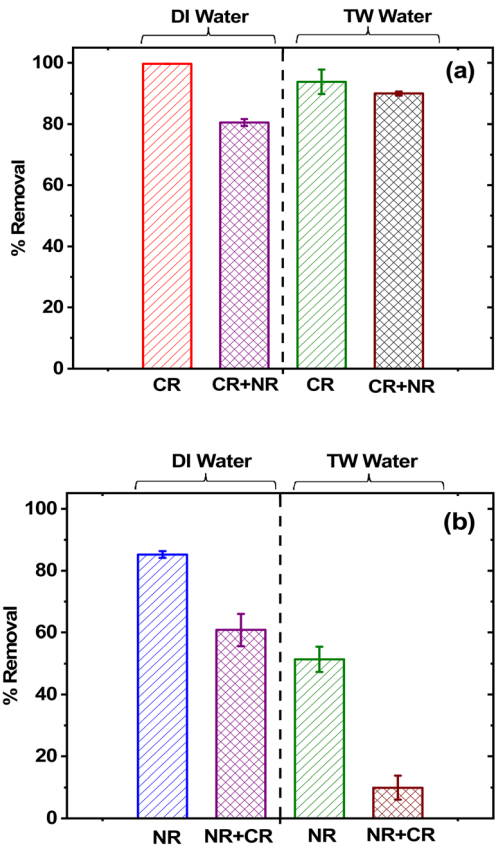

Fig. 9 The comparative (a) CR and (b) NR dye removal efficiency study.

An interesting trend emerged in the binary system (CR + NR). When tested in DI water, the removal efficiency dropped to 80.54 ± 1.16%, indicating a clear competitive effect between the two dyes. However, surprisingly, the binary system in textile wastewater showed improved performance at 90.05 ± 0.66%. The smaller error bar in this condition (*i.e.*, compared to CR alone in textile wastewater) suggests that the binary system achieves more consistent removal in textile wastewater despite the complex matrix. This could be attributed to the higher ionic strength and dissolved solids in textile wastewater (TDS = 329 mg L^{-1}), facilitating a more stable adsorption process. This suggests that while the complex matrix of textile wastewater may introduce variability in single-dye systems, it might help stabilize the removal process in binary systems, possibly through mechanisms involving the wastewater's higher conductivity (*i.e.*, 658 μS cm^{-1}) and altered surface chemistry due to dissolved organics (COD = 238 mg L^{-1}).

Fig. 9(b) represents significant variations in NR removal efficiency across different conditions at pH 11. In the single-dye system using DI water, NR demonstrated the highest removal efficiency of 85.77 ± 1.51%, with the small error bar indicating highly consistent performance. However, when the same concentration was tested in textile wastewater, the removal efficiency decreased substantially to 51.41 ± 4.1%. This decline can be attributed to the complex matrix of textile wastewater, characterized by high TDS, COD, and conductivity. Introducing a competing dye (CR) in the binary system led to further performance deterioration, with removal efficiency dropping to 60.83 ± 5.18% in DI water and dramatically falling to 9.93 ± 3.83% in textile wastewater. The progressively larger error bars in more complex systems (binary and textile wastewater conditions) suggest increasingly variable removal mechanisms, likely due to competitive interactions and matrix effects. The most striking observation is the severe impact of combining both challenges (binary system in textile wastewater), which resulted in a removal efficiency reduction of over 75% compared to the ideal conditions (single dye in DI water). This comprehensive analysis indicates that while NR removal can be highly effective in controlled conditions at pH 11, its performance is significantly compromised by the presence of competing dyes and the complex matrix of textile wastewater, with the combination of these factors resulting in severely reduced removal efficiency.

3.8 Mechanistic understanding of adsorption mechanism

The removal efficiency of CR in DI water was found to be high (~100%) in the presence of positively charged +0.18 mV M-hBN; as shown in Fig. 3(a). This is attributed to the positively charged sites forming on the M-hBN surface, enabling strong electrostatic attractions with the anionic CR dye. At neutral pH (~7.0), the zeta potential decreases to −22.5 mV, significantly reducing the removal efficiency (~20%). This is due to the negatively charged surface repelling the anionic dye molecules, limiting their adsorption. Under alkaline conditions (pH 11), the zeta potential becomes even more negative (−42.8 mV), and the removal efficiency remains low (~20%). The abundance of hydroxyl ions further strengthens the repulsion between the dye molecules and the negatively charged adsorbent surface, preventing effective removal. NR removal efficiency in DI water was 35% at neutral pH (~7.0) with negatively charged M-hBN (−22.5 mV), per Fig. 3(a). From pH 7.0 to 2.0, efficiency remains ~35%, indicating protonation has minimal impact due to saturated adsorbent sites. At pH 11.0, hydroxyl ions and a more negative surface charge (−42.0 mV) increase NR removal to 85%. Beyond pH 2 for CR, pH 11 for NR, or an increase in adsorbent dosage above 0.5 mg L^{-1}, efficiency gains were negligible, as shown in Fig. 3(a) and 4(b).

In brief, the adsorption of CR and NR by M-hBN is driven by electrostatic interactions, hydrogen bonding, and π–π stacking, influenced by pH and material characteristics. Removal efficiencies of 99.23% for CR at pH 2 and 85.77% for NR at pH 11, with adsorption capacities of 620.59 mg g^{-1} and 559.39 mg g^{-1}, respectively, reflect the enhanced performance of M-hBN over pristine h-BN. These outcomes result from hydroxyl groups and structural defects introduced during NaOH-based chemical weathering. Liu *et al.* (2014) reported enhanced methylene blue

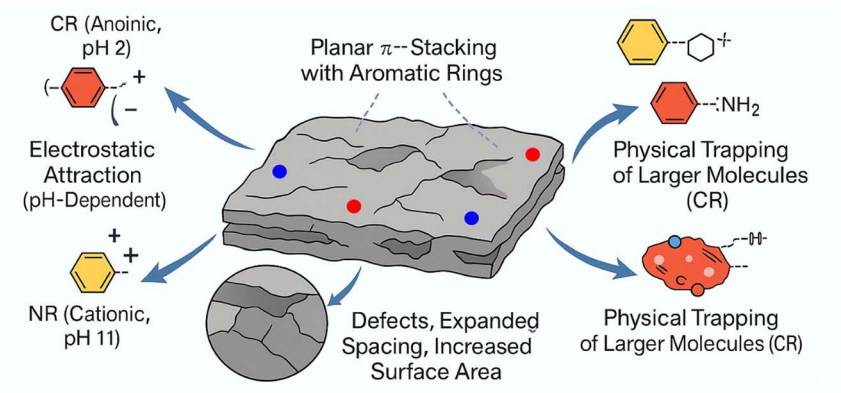

Fig. 10 Dye removal adsorption mechanism.

adsorption by hydroxylated h-BN, driven by polarity and hydrogen bonding.[10] Bhattacharya *et al.* (2012) reported increased reactivity of hydroxyl-functionalized h-BN, supporting its role in dye binding.[61] Lei *et al.* (2013) and Wang *et al.* (2018) reported enhanced CR and RhB adsorption, respectively, by defect-rich h-BN nanosheets, attributed to increased surface area and porosity.[18,82]

The superior capacities and Langmuir fit highlight the synergy of these features, distinguishing M-hBN from pristine h-BN and literature benchmarks. Similar dye removal results, highlighting chemisorption, Langmuir isotherm behavior, and the influence of surface charge on pH, were reported for various adsorbents, such as BNNS, iron nanoparticles, porous boron nitride nanosheets, and functional 3D boron nitride architectures for the removal of dyes such as MB, RhB, MO, CR, and BY from wastewater[6,10,31,83,84] and functional boron nitride, Fe_3O_4 hollow nanospheres, halloysite nanotubes, and BNNS for the removal of dyes such as NR, MB, and RhB.[6,68,77,85]

In summary, the exceptional adsorption capacity observed can be attributed to two primary factors: (i) the structural compatibility between the planar morphology of M-hBN and the aromatic ring configurations present in both CR and NR molecules, facilitating strong π–π stacking interactions; and (ii) pH-dependent electrostatic interactions between the charged surface of M-hBN and the respective ionic states of the dyes, *i.e.*, anionic CR and cationic NR; and (iii) the structural defects provide increased surface area, exposed boron/nitrogen sties, and possible physical trapping for dye molecules. This synergistic combination of non-covalent π–π interactions and electrostatic forces with structurally modified nanoparticles, depicted in Fig. 10, results in enhanced adsorption efficiency of dyes.

4 Conclusion

Structurally modified h-BN effectively removed dyes under different medium conditions and dye compositions. The dye removal efficiency varied across media, peaking in DI water for CR (99.23 ± 0.06%) and retaining 91.49 ± 1.31% (CR) and 75.89 ± 0.50% (NR) after seven cycles, underscoring reusability. Adsorption adhered to a pseudo-second-order kinetic model, suggesting chemisorption as the dominant mechanism, and followed the Langmuir isotherm, indicating monolayer coverage. The process relied primarily on –OH interactions with dye ions, augmented by pore diffusion and π–π stacking, enabling selective removal based on ionic properties. This study positions modified h-BN as a promising adsorbent for anionic and cationic dyes in industrial wastewater treatment. Further investigation into BN derivative toxicity, cost-effective functionalization, pilot-scale optimization, and simultaneous removal of heavy metals and antibiotics in real textile effluents will enhance its practical applicability and scalability.

Author contributions

A. A. N.: conceptualization; investigation; methodology; validation; writing – original draft, K. N. S.: data curation; visualization, Z. B. Z. S.: writing – review & editing, M. K. A.: resources; writing – review & editing, S. A.: resources; writing – review & editing, I. A. K.: conceptualization; supervision; project administration; writing – review & editing.

Conflicts of interest

The authors declare that they have no known competing financial interests or personal relationships that could have appeared to influence the work reported in this paper.

Data availability

The corresponding author will make available all calculations upon request.

The data supporting this article have been included as part of the SI. See DOI: **https://doi.org/10.1039/d5ra03754a**.

Acknowledgements

The authors would like to acknowledge the support from the Department of Chemical Engineering and the Department of Physics, Bangladesh University of Engineering and Technology (BUET). The authors also acknowledge the Committee for Advanced Studies & Research (CASR), BUET, for providing the funds to execute this research.

References

1 M. A. Minhas, A. Rauf, S. Rauf, F. T. Minhas, N. Memon, A. Jabbar, M. I. Bhanger and M. I. Malik, *Sep. Purif. Technol.*, 2021, **272**, 118883.
2 A. Ghaly, R. Ananthashankar, M. Alhattab and V. V. Ramakrishnan, *J. Chem. Eng. Process Technol.*, 2014, **5**, 1–19.
3 I. Laing, *Rev. Prog. Coloration Relat. Top.*, 1991, **21**, 56–71.
4 B. Lellis, C. Z. Fávaro-Polonio, J. A. Pamphile and J. C. Polonio, *Biotechnol. Res. Innov.*, 2019, **3**, 275–290.
5 R. Al-Tohamy, S. S. Ali, F. Li, K. M. Okasha, Y. A.-G. Mahmoud, T. Elsamahy, H. Jiao, Y. Fu and J. Sun, *Ecotoxicol. Environ. Saf.*, 2022, **231**, 113160.
6 R. S. Bangari and N. Sinha, *J. Nanosci. Nanotechnol.*, 2020, **20**, 6222–6234.
7 Y. Guo, R. Wang, P. Wang, L. Rao and C. Wang, *ACS Sustain. Chem. Eng.*, 2019, **7**, 5727–5741.
8 J. Li, Y. Huang, Z. Liu, J. Zhang, X. Liu, H. Luo, Y. Ma, X. Xu, Y. Lu, J. Lin, J. Zou and C. Tang, *J. Mater. Chem. A*, 2015, **3**, 8185–8193.
9 Q. Li, T. Yang, Q. Yang, F. Wang, K.-C. Chou and X. Hou, *Ceram. Int.*, 2016, **42**, 8754–8762.
10 D. Liu, W. Lei, S. Qin and Y. Chen, *Sci. Rep.*, 2014, **4**, 4453.
11 F. Liu, Q. Zhou, Y. Li and J. Pang, *Nanomaterials*, 2022, **12**(3), 318.
12 Z. Liu, Y. Fang, H. Jia, C. Wang, Q. Song, L. Li, J. Lin, Y. Huang, C. Yu and C. Tang, *Sci. Rep.*, 2018, **8**, 1104.

13 J. Pang, Y. Chao, H. Chang, H. Li, J. Xiong, Q. Zhang, G. Chen, J. Qian, W. Zhu and H. Li, *ACS Sustain. Chem. Eng.*, 2018, **6**, 4948–4957.
14 M. Ptaszkowska-Koniarz, J. Goscianska and R. Pietrzak, *J. Colloid Interface Sci.*, 2017, **504**, 549–560.
15 T. Shen, S. Liu, W. Yan and J. Wang, *J. Mater. Sci.*, 2019, **54**, 8852–8859.
16 V. Ugraskan, B. Isik and O. Yazici, *Chem. Eng. Commun.*, 2022, **209**, 1111–1129.
17 N. Vázquez-Canales and J. García-Serrano, *Sustain. Chem. Environ.*, 2025, **9**, 100193.
18 X. Wang, Y. Yang, G. Jiang, Z. Yuan and S. Yuan, *Diamond Relat. Mater.*, 2018, **81**, 89–95.
19 C. Xu, J. Zeng, X. Gu, Y. Wang, E. Li, C. Zhang, C. Ge, C. Jin, M. Miao, Z. Jin, T. Gao, X. Jiang, P. Dai, Y. Bando, R. Li, J. Rong and X.-B. Wang, *J. Mater. Chem. A*, 2022, **10**, 846–854.
20 C. Yang, D. Bu and S. Huang, *Ceram. Int.*, 2022, **48**, 27658–27663.
21 T. Attar, A. Benchadli, B. Messaoudi and E. Choukchou-Braham, *Chem. Chem. Technol.*, 2022, **16**, 440–447.
22 M. Singh, H. Pal and A. Sapre, *Photochem. Photobiol.*, 2000, **71**, 44–52.
23 G. Z. Kyzas, M. Kostoglou, N. K. Lazaridis and D. N. Bikiaris, *Eco-Friendly Textile Dyeing and Finishing*, ed. M. Günay, Intech, 2013, pp. 177–206.
24 A. Tabak, E. Eren, B. Afsin and B. Caglar, *J. Hazard. Mater.*, 2009, **161**, 1087–1094.
25 M. A. M. Salleh, D. K. Mahmoud, W. A. W. A. Karim and A. Idris, *Desalination*, 2011, **280**, 1–13.
26 I. Ihsanullah, *Chemosphere*, 2021, **263**, 127970.
27 M. Mehta, M. Sharma, K. Pathania, P. K. Jena and I. Bhushan, *Environ. Sci. Pollut. Res.*, 2021, **28**, 49434–49446.
28 B. Bhushan, A. Nayak, G. Bhatnagar, A. Chauhan and D. Kashyap, *J. Water Proc. Eng.*, 2024, **66**, 105916.
29 Q. Weng, X. Wang, X. Wang, Y. Bando and D. Golberg, *Chem. Soc. Rev.*, 2016, **45**, 3989–4012.
30 C. Martínez-Jiménez, A. Chow, A. D. S. McWilliams and A. A. Martí, *Nanoscale*, 2023, **15**, 16836–16873.
31 R. S. Bangari, A. Yadav and N. Sinha, *Soft Matter*, 2021, **17**, 2640–2651.
32 J. Li, S. He, R. Li, W. Dai, J. Tao, C. Wang, J. Liu, T. Wu and C. Tang, *RSC Adv.*, 2018, **8**, 32886–32892.
33 D.-H. Jiang, P.-C. Chiu, C.-J. Cho, L. Veeramuthu, S.-H. Tung, T. Satoh, W.-H. Chiang, X. Cai and C.-C. Kuo, *Nanomaterials*, 2019, **9**, 1383.
34 H. Li, S. Zhu, M. Zhang, P. Wu, J. Pang, W. Zhu, W. Jiang and H. Li, *ACS Omega*, 2017, **2**, 5385–5394.
35 J. Li, X. Xiao, X. Xu, J. Lin, Y. Huang, Y. Xue, P. Jin, J. Zou and C. Tang, *Sci. Rep.*, 2013, **3**, 3208.
36 G. Constantinescu, A. Kuc and T. Heine, *Phys. Rev. Lett.*, 2013, **111**, 036104.
37 J. Di, J. Xia, M. Ji, B. Wang, S. Yin, Q. Zhang, Z. Chen and H. Li, *Appl. Catal., B*, 2016, **183**, 254–262.
38 H. Fang, S.-L. Bai and C. P. Wong, *Compos. Commun.*, 2016, **2**, 19–24.
39 Z. Sun, L. Lin, M. Yuan, H. Li, G. Sun, S. Ma and X. Yang, *Nanotechnology*, 2018, **29**, 215602.
40 G. Zhao, F. Zhang, Y. Wu, X. Hao, Z. Wang and X. Xu, *Adv. Opt. Mater.*, 2016, **4**, 141–146.
41 Z.-S. Ma, H.-L. Ding, Z. Liu and Z.-L. Cheng, *J. Alloys Compd.*, 2019, **784**, 807–815.
42 J. Li, C. Wang, X. Chen, Y. Ma, C. Dai, H. Yang, Q. Li, J. Tao and T. Wu, *RSC Adv.*, 2024, **14**, 7124–7130.
43 Q. Song, Y. Fang, J. Wang, J. Liang, Q. Hu, Z. Liu, Y. Huang, Y. Xue, J. Lin and C. Tang, *J. Alloys Compd.*, 2019, **793**, 512–518.
44 R. S. Bangari, V. K. Yadav, J. K. Singh and N. Sinha, *ACS Omega*, 2020, **5**, 10301–10314.
45 P. Bartczak, M. Wawrzkiewicz, S. Borysiak and T. Jesionowski, *Processes*, 2022, **10**, 586.
46 E. D. Revellame, D. L. Fortela, W. Sharp, R. Hernandez and M. E. Zappi, *Clean Eng. Technol.*, 2020, **1**, 100032.
47 R. K. Khamizov, *Russ. J. Phys. Chem. A*, 2020, **94**, 171–176.
48 W. J. Weber Jr and J. C. Morris, *J. Sanit. Eng. Div.*, 1963, **89**, 31–59.
49 C. E. Almeida-Naranjo, M. B. Aldás, G. Cabrera and V. H. Guerrero, *Environ. Chall.*, 2021, **5**, 100343.
50 X. Song, Y. Zhang, C. Yan, W. Jiang and C. Chang, *J. Colloid Interface Sci.*, 2013, **389**, 213–219.
51 O. P. Murphy, M. Vashishtha, P. Palanisamy and K. V. Kumar, *ACS Omega*, 2023, **8**, 17407–17430.
52 N. Kumara, N. Hamdan, M. I. Petra, K. U. Tennakoon and P. Ekanayake, *J. Chem.*, 2014, **2014**, 468975.
53 D. Balarak, J. Jaafari, G. Hassani, Y. Mahdavi, I. Tyagi, S. Agarwal and V. K. Gupta, *Colloids Interface Sci. Commun.*, 2015, **7**, 16–19.
54 H. Roy, S. H. Firoz, M. M. K. Bhuiyan and M. S. Islam, *J. Water Proc. Eng.*, 2024, **68**, 106295.
55 A. A. Mizhir, A. A. Abdulwahid and H. S. Al-Lami, *Desalin. Water Treat.*, 2020, **202**, 381–395.
56 M. S. Islam, H. Roy, T. Ahmed, S. H. Firoz and S. X. Chang, *Chemosphere*, 2023, **340**, 139827.
57 B. Zhang, Q. Wu, H. Yu, C. Bulin, H. Sun, R. Li, X. Ge and R. Xing, *Nanoscale Res. Lett.*, 2017, **12**, 596.
58 H. Wang, X. Su, T. Song, Z. Li, Y. Zhao, H. Lou and J. Wang, *Appl. Surf. Sci.*, 2019, **488**, 656–661.
59 C. Zhi, Y. Bando, C. Tang, H. Kuwahara and D. Golberg, *Adv. Mater.*, 2009, **21**, 2889–2893.
60 G. Zhao, F. Zhang, Y. Wu, X. Hao, Z. Wang and X. Xu, *Adv. Opt. Mater.*, 2016, **4**, 141–146.
61 A. Bhattacharya, S. Bhattacharya and G. P. Das, *Phys. Rev. B: Condens. Matter Mater. Phys.*, 2012, **85**, 035415.
62 V. Guerra, C. Wan, V. Degirmenci, J. Sloan, D. Presvytis and T. McNally, *Nanoscale*, 2018, **10**, 19469–19477.
63 A. S. Nazarov, V. N. Demin, E. D. Grayfer, A. I. Bulavchenko, A. T. Arymbaeva, H. J. Shin, J. Y. Choi and V. E. Fedorov, *Chem.–Asian J.*, 2012, **7**, 554–560.
64 L. Cao, S. Emami and K. Lafdi, *Mater. Express*, 2014, **4**, 165–171.
65 J. Ren, L. Stagi and P. Innocenzi, *J. Mater. Sci.*, 2021, **56**, 4053–4079.
66 T. Sainsbury, A. Satti, P. May, Z. Wang, I. McGovern, Y. K. Gun'ko and J. Coleman, *J. Am. Chem. Soc.*, 2012, **134**, 18758–18771.

67 M.-X. Zhu, L. Lee, H.-H. Wang and Z. Wang, *J. Hazard. Mater.*, 2007, **149**, 735–741.
68 P. Luo, Y. Zhao, B. Zhang, J. Liu, Y. Yang and J. Liu, *Water Res.*, 2010, **44**, 1489–1497.
69 S. S. Ahluwalia and D. Goyal, *Bioresour. Technol.*, 2007, **98**, 2243–2257.
70 D. Dimbo, M. Abewaa, E. Adino, A. Mengistu, T. Takele, A. Oro and M. Rangaraju, *Results Eng.*, 2024, **21**, 101910.
71 S. Chawla, H. Uppal, M. Yadav, N. Bahadur and N. Singh, *Ecotoxicol. Environ. Saf.*, 2017, **135**, 68–74.
72 A. Elsagh, O. Moradi, A. Fakhri, F. Najafi, R. Alizadeh and V. Haddadi, *Arab. J. Chem.*, 2017, **10**, S2862–S2869.
73 A. Soltani, M. Faramarzi and S. A. Mousavi Parsa, *Water Qual. Res. J.*, 2021, **56**, 181–193.
74 E. Lorenc-Grabowska and G. Gryglewicz, *Dyes Pigm.*, 2007, **74**, 34–40.
75 V. Vimonses, S. Lei, B. Jin, C. W. K. Chow and C. Saint, *Chem. Eng. J.*, 2009, **148**, 354–364.
76 S. Al-Salihi, A. M. Jasim, M. M. Fidalgo and Y. Xing, *Chemosphere*, 2022, **286**, 131769.
77 M. Iram, C. Guo, Y. Guan, A. Ishfaq and H. Liu, *J. Hazard. Mater.*, 2010, **181**, 1039–1050.
78 J. Zhang, Q. Shi, C. Zhang, J. Xu, B. Zhai and B. Zhang, *Bioresour. Technol.*, 2008, **99**, 8974–8980.
79 R. Li, W. Sun, L. Xia, Z. U, X. Sun, Z. Wang, Y. Wang and X. Deng, *Molecules*, 2022, **27**, 7980.
80 K. O. Yoro, M. K. Amosa, P. T. Sekoai, J. Mulopo and M. O. Daramola, *Int. J. Sustain. Eng.*, 2020, **13**, 54–67.
81 E. N. El Qada, S. J. Allen and G. M. Walker, *Chem. Eng. J.*, 2006, **124**, 103–110.
82 W. Lei, D. Portehault, D. Liu, S. Qin and Y. Chen, *Nat. Commun.*, 2013, **4**, 1777.
83 S. Ghorai, A. K. Sarkar, A. B. Panda and S. Pal, *Bioresour. Technol.*, 2013, **144**, 485–491.
84 S.-H. Kim and P.-P. Choi, *Dalton Trans.*, 2017, **46**, 15470–15479.
85 T. Zheng, Y. Xu, C. Yan, S. Zhang, Y. Guo and S. Hua, *Mater. Res. Express*, 2019, **6**, 0950a0951.